

78 0148

ADA132393

CHARACTERIZATION OF ELECTRICALLY ACTIVE
DEFECTS IN SI USING CCD IMAGE SENSORS

H. F. Schaake
C. G. Roberts
A. J. Lewis

Texas Instruments Incorporated

January 1978

Quarterly Technical Report
1 September 1977 - 30 November 1977

APPROVED FOR PUBLIC RELEASE
DISTRIBUTION UNLIMITED

Sponsored by
Advanced Research Projects Agency
ARPA Order No. 3219

DTIC
ELECTE
S SEP 13 1983 D
B

The views and conclusions contained in this document are those of the authors and should not be interpreted as necessarily representing the official policies, either expressed or implied, of the Advanced Research Projects Agency of the U. S. Government.

DTIC FILE COPY

83 09 01 064

TI Report No.
08-78-03

QUARTERLY TECHNICAL REPORT
CONTRACT NO. NO0173-76-C-0280
1 September 1977 - 30 November 1977

Sponsored by
Advanced Research Projects Agency
ARPA Order No. 3219

ARPA Order Number: 3219
Program Code Number: 6D10
Name of Contractor: Texas Instruments Incorporated
Central Research Laboratories
P. O. Box 5936
Dallas, Texas 75222
Effective Date of Contract: 30 July 1976
Contract Expiration Date: 30 March 1978
Amount of Contract: \$205,329.00
Contract Number: NO0173-76-C-0280
Principal Investigator and Phone No.: Dr. H. F. Schaafe
(214) 238-4204
Scientific Officer and Phone No.: Dr. Dave Barbe - Code 5260
Naval Research Laboratory
(202) 767-2408
Short Title of Work: Characterization of Electrically
Active Defects in Si Using CCD
Image Sensors

The views and conclusions contained in this document are those of the authors and should not be interpreted as necessarily representing the official policies, either expressed or implied, of the Advanced Research Projects Agency or the U. S. Government.

DISTRIBUTION STATEMENT A

Approved for public release
Distribution Unlimited

TABLE OF CONTENTS

<u>SECTION</u>		<u>PAGE</u>
I	INTRODUCTION.	2
II	EXPERIMENTAL RESULTS.	4
	A. Czochralski - Control Group.	4
	1. Imager Performance.	4
	2. X-Ray Topography.	4
	3. Transmission Electron Microscopy.	4
	4. Discussion.	11
	B. Float-Zoned Material	13
	1. Imager Performance.	13
	2. X-Ray Topography.	15
	3. Transmission Electron Microscopy.	15
	4. Discussion.	19
	C. Czochralski - Group 1.	26
	1. Imager Performance.	26
	2. X-Ray Topography.	26
	D. Czochralski - Group 2.	29
	1. Imager Performance.	29
	2. X-Ray Topography.	29
	3. Discussion.	32
	E. Czochralski - Group 3.	34
	1. Imager Performance.	34
	2. X-Ray Topography.	34
	3. Transmission Electron Microscopy.	34
	4. Discussion.	36
	F. Results of ISS Backside Damage Tests	36
	G. Relationship of Total Dark Current and Dark Current Spike Density.	43
	H. Role of Transition Metal Impurities.	44
III	DISCUSSION.	46
IV	PLANS	49
	REFERENCES.	50

LIST OF ILLUSTRATIONS

<u>FIGURE</u>		<u>PAGE</u>
1	Dark Current Patterns: Czochralski - Control Group	5
2	(220) Transmission Topograph of Wafer From Czochralski - Control Group	6
3	TEM Micrographs of Defects in Czochralski - Control Group Devices	7
4	Distribution of Defects in Czochralski - Control Group. . .	9
5	Weak Beam (400) Micrograph of Pure Edge Dislocation in Czochralski - Control Group	10
6	Dark Current Patterns - Float-Zoned Group	14
7	(220) Transmission Topograph of Float-Zoned Wafer Showing Damage Near Center.	16
8	Enlargement of (220) Transmission Topograph Showing Dislocations Emanating From Backside-Damaged Regions. . . .	17
9	Enlargement of (224) Reflection Topograph of Dislocated Region in Float-Zoned Region.	18
10	Transmission Electron Micrograph of 60° Dislocations Near Front Surface of Float-Zoned Wafer	20
11	Dark Field Transmission Electron Micrograph of Float-Zoned Wafer Showing Dislocation Reaction.	21
12	Weak Beam (400) Micrograph of Partially Dissociated Dislocation	22
13	Transmission Electron Micrograph of Stacking Fault in Channel Stop of Float-Zoned Wafer	23
14	Dark Current Patterns - Czochralski Group 1	27
15	(224) Reflection Topographs of Defects in Czochralski Group 1	28
16	Dark Current Patterns of Three Adjacent Devices, Czochralski Group 2	30
17	224 Reflection Topograph of Dark Current Defects in Czochralski Group 2	31
18	(220) Transmission Topograph of Two Devices Whose Dark Current Signature Is Shown in Figure 16	33
19	Dark Current Pattern in Czochralski Group 3	35
20	Dislocation Clusters in Channel Stop Region	37

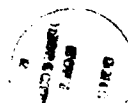
LIST OF ILLUSTRATIONS

(continued)

<u>FIGURE</u>		<u>PAGE</u>
21	Defects in Channel Region	38
22	(220) Transmission Topograph Showing Pattern of ISS Backside Damage	40
23	Dark Current Readout of Typical Devices on Control Slices Not Treated with ISS.	41
24	Dark Current Readout of Typical Devices from Slices Treated with the ISS Backside Damage.	42

DTIC
ELECTE
S SEP 13 1983 **D**
B

Accession For	
NTIS GRA&I	<input checked="" type="checkbox"/>
DTIC TAB	<input type="checkbox"/>
Unannounced	<input type="checkbox"/>
Justification	
By _____	
Distribution/	
Availability Codes	
Dist	Avail and/or Special
A	



TECHNICAL REPORT SUMMARY

During the past quarter, work has progressed on the characterization of the sources of dark current spikes in the imagers whose operation was previously reported. Three classes of defects with five specific origins have been observed to cause dark current spikes:

(1) Dislocations from thermal stresses or device stresses, or from the unfaulting of a stacking fault whose origin is bulk nucleation.

(2) Stacking faults nucleated from surface scratches, or by another surface mechanism.

(3) A surface/interface defect that has not yet been identified.

Only two of these defects (surface/interface defect and stacking faults nucleated from the surface) are getterable by backside damage.

A good correlation was found between imagers relatively free of dark current spikes and regions of a wafer where swirl precipitation of oxygen occurred in the bulk. Dark current spikes from unfaulted bulk dislocations and clusters of dislocations from device stress were found in some of these imagers, however, indicating that they are not "getterred" by the bulk swirl precipitation.

It has also been found by high resolution transmission electron microscopy in the "weak-beam" mode that slip dislocations are at least partially dissociated into two partial dislocations, while dislocations arising from the unfaulting of a stacking fault are not dissociated. The electrical activity of these defects suggests a model in which dark current spike activity of dislocations arises only from regions of a dislocation that are not dissociated. No impurity precipitates have been observed in the depletion region of any device.

SECTION I
INTRODUCTION

During the past quarter, the CCD imagers whose electrical performance was reported in the last quarterly report were extensively studied by x-ray topography and transmission electron microscopy. Installation of the new JEOL-100CX Scanning Transmission Electron Microscope (STEM) has been completed, and this powerful new instrument is available for characterization studies of defects in CCD imagers. As discussed subsequently in this report, this new instrument has already provided new insights into the nature of dislocations in CCD imagers.

As reported in the last Quarterly Technical Report,¹ we had not seen a correlation between dark current spikes in a moderate to high density, and defects imaged in x-ray topography. This continues to be the case. Electron microscopic examination of these imagers reveals that this is so because the defects are micrometer or submicrometer dislocations or stacking faults, which are too small for the limited resolution of x-ray topography.

The correlations that could be made between dark current spikes and defects observable in transmission electron microscopy have been statistical so far. That is, the number of visible defects of a type observable in the electron microscope is correlated with the number of dark current spikes observable in the region of the imager from which the sample was taken. This is an adequate technique when 1% or more of the pixels contain dark current spikes. This approach has enabled us to look at a larger number of specimens for each material, and therefore to obtain a better idea of the total defect picture in the material. In the coming quarter we plan to attempt some one-to-one correlations between the video image and transmission electron micrographs for microscopic ($< 1 \mu\text{m}$) defects.

Section II of this report presents the result of experiments for each group of materials that is being used. Also included in Section II are observations on the effectiveness of ISS backside damage, the relationship between total dark current and dark current spike density, and a discussion of the absence of any effects from transition metal impurities. The final section of this report discusses the origin of these defects and what may be done to eliminate them. —

SECTION II

EXPERIMENTAL RESULTS

All starting material reported on in this section is 3 inch diameter (76.2 mm), p-type, 8 to 15 Ω -cm Czochralski (pulled in Varian pullers), or float-zoned silicon with (100) surface orientation. The Czochralski material was obtained from TI, while the float-zoned material was obtained from Wacker. With the exception of Czochralski Group III, all wafers had $\langle 110 \rangle$ flats.

A. Czochralski - Control Group

These slices were taken from a group of control material to determine the consistency of the processing.

1. Imager Performance

A typical dark current pattern observed in devices made on this material is shown in Figure 1. The random distribution of dark current spikes illustrated in this figure is typical of all imagers that were operated on the slice.

2. X-Ray Topography

Very few defects were imaged in both reflection and transmission x-ray topography. Consequently, there is no correlation between the predominant dark current producing defect and defects visible in x-ray topography. However, transmission topography showed that the bulk of the slice contained a uniform "swirl" precipitate (Figure 2).

3. Transmission Electron Microscopy

Samples for transmission electron microscopy were taken from regions of imagers that showed the highest density of defects. Typical defects seen in this material are illustrated in Figure 3. Stacking faults [Figure 3(a) and 3(b)] were seen only in the channel stops. Approximately 90% of these

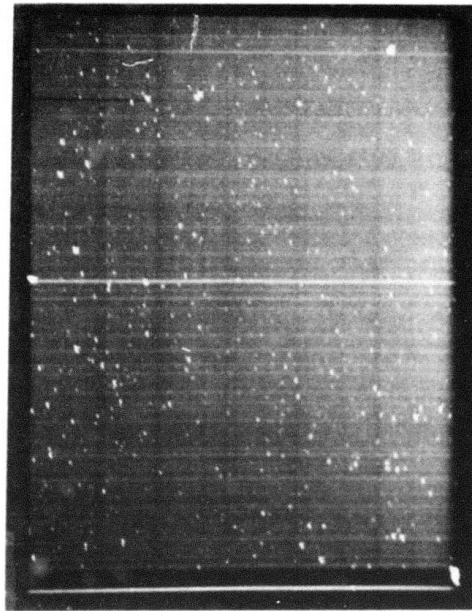


Figure 1 Dark Current Patterns: Czochralski - Control Group

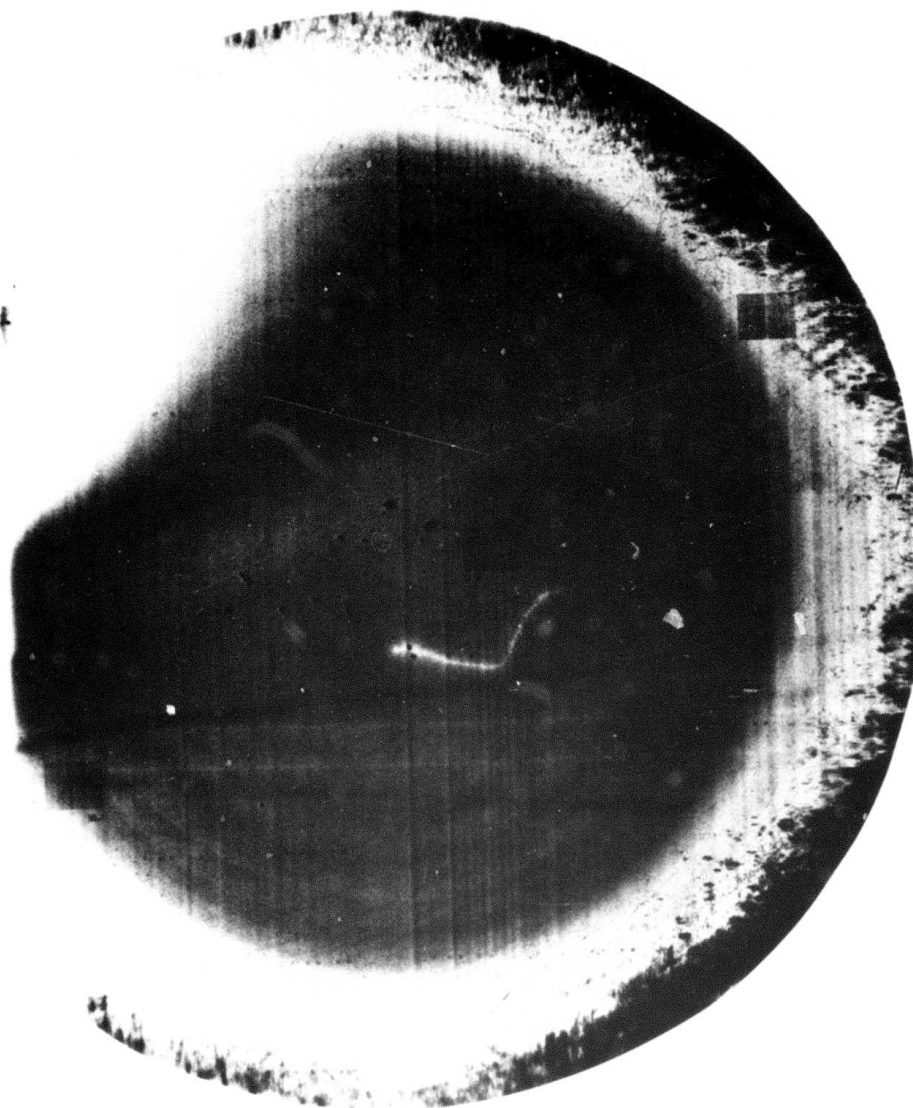


Figure 2 (220) Transmission Topograph of Wafer from Czochralski - Control Group.
Note bulk swirl precipitation region covering most of the slice.

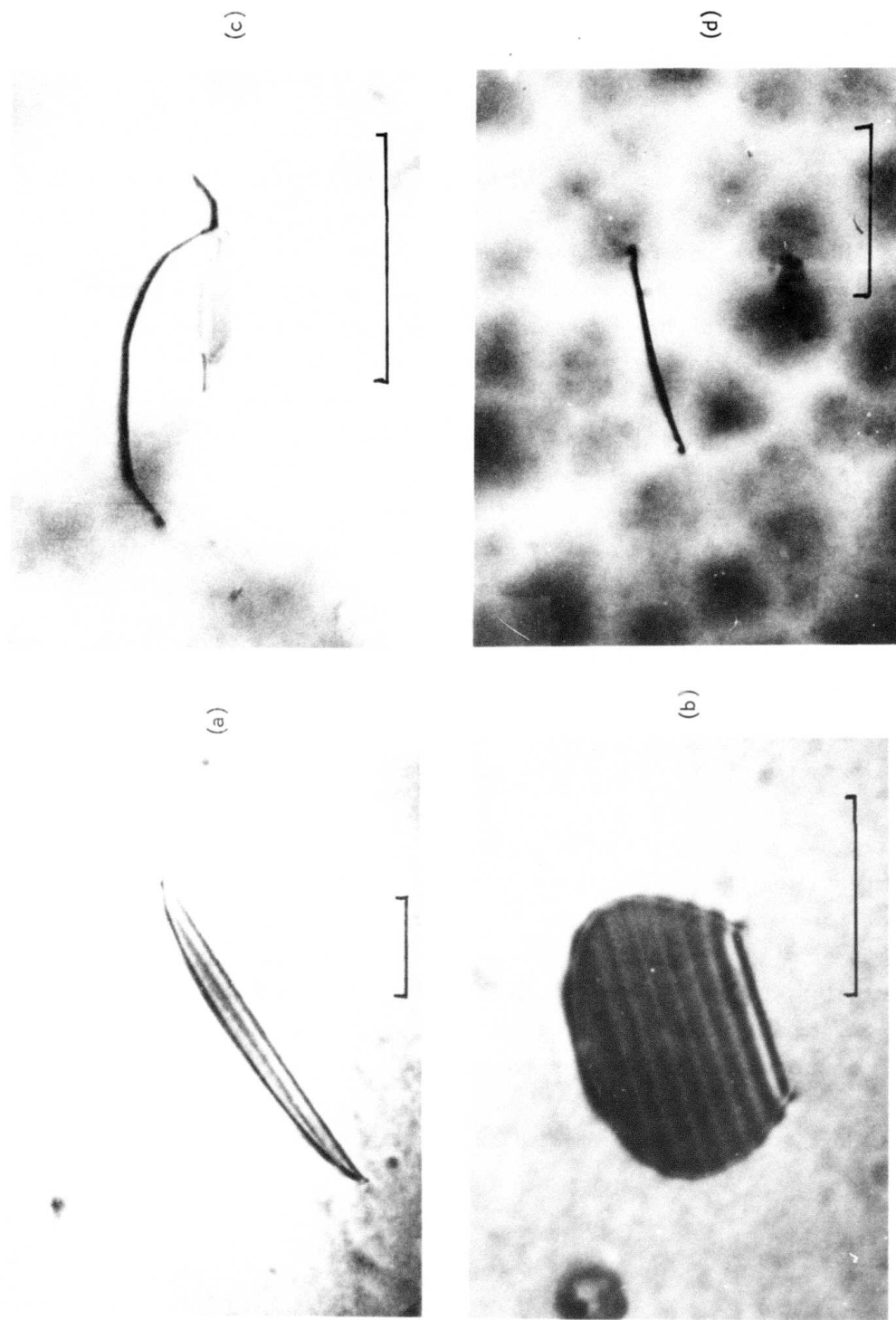


Figure 3 TEM Micrographs of Defects in Czochralski - Control Group Devices. (a) and (b), stacking faults in channel stops; (c) and (d), dislocations in channels. All markers = 0.5 μm .

stacking faults were found to be located underneath the polysilicon gate (Figure 4). The length of the stacking faults varied from approximately $0.5\text{ }\mu\text{m}$ to $10\text{ }\mu\text{m}$. Most were under $1\text{ }\mu\text{m}$ in length. Dislocation loops were found in both the channels and channel stops. These loops were invariably oriented in a $\langle 110 \rangle$ direction. In the channels they were found to be oriented only in a direction perpendicular to the channels and channel stops. All the dislocations in the channels were found at the edge of the polysilicon gate (Figure 4). In the channel stops they were oriented either in this same direction or in a direction perpendicular to the channels and channel stops. Contrast experiments in the electron microscope showed that all these dislocations were pure edge dislocations [i.e., the Burgers vector was perpendicular to the dislocation line, and in the (001) plane of the surface of the slice]. The density of the dislocations in the channels was found to be approximately the same as the density of dark current spikes in the imager. The density of stacking faults in the channel stops was considerably larger. (To date, we have observed six dislocations in the channels, and approximately 30 stacking faults and dislocations in the channel stops.)

Since the installation of the new STEM, we have examined these dislocations using the weak beam technique of Ray and Cockayne.² In this technique the sample is tilted so that the Bragg reflection of interest is only weakly excited. The diffracted beam is then imaged. As a result of the weak excitation, the dislocation width is substantially reduced. For example, the image width in normal microscopy is of the order of $100\text{ }\text{\AA}$, while in the weak beam technique, it may be as small as $10\text{ }\text{\AA}$. Consequently, it is possible to see if the perfect dislocation is dissociated into two partial dislocations. Our results consistently show that these dislocations are not dissociated (Figure 5).





Channel Stop			
Channel			
	Polysilicon	Aluminum	

Figure 4 Distribution of Defects in Czochralski - Control Group. Stacking faults in channel stops, and dislocation loops in channels, both predominantly under the polysilicon electrode.



20 nm

Figure 5 Weak Beam (400) Micrograph of Pure Edge Dislocation in Czochralski - Control Group. The dislocation is not dissociated.

4. Discussion

This discussion will be confined to the origin of the stacking faults and dislocations. Although it certainly appears that the small dislocations are the source of dark current spikes in these devices, the reason this is so will be discussed in a later section.

Dislocations such as those seen in Figure 3 cannot originate by a simple glide mechanism; that is, they cannot originate at some point in the crystal and move by slip to their present position because the plane containing both the dislocation line and the Burgers vector of the dislocation is a (100) plane and not a slip plane, which must be of the type (111). There are three mechanisms by which these pure edge dislocations may form: (1) through the unfauling of a stacking fault, (2) through the formation of the dislocation at the surface and the subsequent climb of the dislocation by the emission or absorption of silicon interstitials or vacancies, and (3) through a dislocation reaction such as $\frac{1}{2}\langle 10\bar{1} \rangle \rightarrow \frac{1}{2}\langle 1\bar{1}0 \rangle + \frac{1}{2}\langle 01\bar{1} \rangle$. Of these mechanisms, the first seems the most probable, since stacking faults are seen in other portions of the crystal, and since the dislocation in Figure 3(c) has the same shape as the partial dislocation bounding a stacking fault [compare with Figure 3(a)]. As we have previously observed, the majority of dislocations that result from the unfauling of a stacking fault are pure edge in nature.³ We conclude that all the defects seen in this device originate from the same source, namely, the growth of a stacking fault.

With regard to the origin of the stacking faults, the literature recognizes two types of stacking faults (see, for example, Reference 4): surface or oxidation induced, and bulk. Surface stacking faults can be nucleated from a scratch³ or from an as-yet unidentified, but getterable, mechanism. Their characteristic is that they begin to grow as soon as oxidation commences, and they continue to grow throughout an oxidation cycle.

During a nonoxidizing cycle, they shrink at a rate dependent on whether or not there is a thermal oxide overlying the stacking fault.^{5,6} Thus, the size of the stacking faults is dependent only on the local processing. If surface nucleation were the cause of the stacking faults we observe, we should see stacking faults about 10 μm long in the channel stop, and somewhat shorter stacking faults in the channel. Since most of the stacking faults we observe are considerably smaller than this, surface nuclei can be reasonably eliminated as the origin of the dislocations we observe.

Our observations further support a bulk origin of the stacking faults. The almost circular stacking fault in Figure 3(b) is typical of a stacking fault that has been growing in the interior of the crystal and has just intersected the surface. It is difficult to explain such a shape from a surface nucleation mechanism. In addition, the size of the majority of the stacking faults is about the same as that of stacking faults we found in the bulk of "swirled" material, which were clearly of bulk origin.¹ We therefore conclude that the stacking faults were nucleated from bulk nuclei.

Next, we consider the distribution of the defects as depicted in Figure 4. Since bulk nuclei are the origin of the stacking faults, we would expect the stacking faults to be found at random throughout the surface region. In fact, there is a device-dependent distribution, as shown in Figure 4. One explanation of this distribution is that the nucleation or growth of the stacking faults required specific conditions that are found only in some portions of the device. Alternatively, the stacking faults could nucleate and grow in all portions of the device, but the processing of the device could favor the removal of the stacking faults in some portions of the device by either a shrinkage or an unfauling mechanism, with subsequent climb of the resulting perfect dislocation out of the crystal. Although current observations cannot make a strong case for either of these mechanisms, our previous observations on bulk stacking faults in "swirled" material¹ strongly

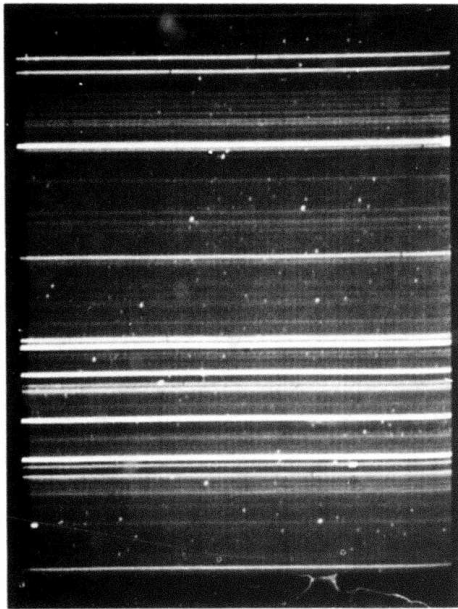
suggest that the requirements for the nucleation and growth of the bulk stacking faults are met everywhere in the device. In this previous work, the size of the observed stacking faults was the same in the bulk underneath both the channels and the channel stops. It thus seems most probable that the second mechanism is responsible for the distribution of defects that is observed. The role of the thick oxide, particularly when it is overlain by polysilicon, is thus to inhibit the unfauling of the stacking faults. In the channel where the oxide is always relatively thin, the unfauling can evidently occur with comparative ease, and the resulting perfect dislocations are able to climb out of the silicon.⁵ The driving force for the climb process is postulated to be the image force induced by the surface. At the edges of the polysilicon, the strain field from the polysilicon is evidently sufficient to inhibit the climb of the dislocations, and it is here that we see the dark current producing defect.

That the resulting perfect dislocations in the channels are not dissociated is in agreement with theory. The only energetically favored dissociation of a perfect dislocation is into two Shockley partials: $1/2\langle 110 \rangle \rightarrow 1/6\langle 21\bar{1} \rangle + 1/6\langle 121 \rangle$. For this reaction to occur, the dislocation line and the Burgers vector of the dislocation must lie on a slip plane. As has already been discussed, this is not the case for these dislocations.

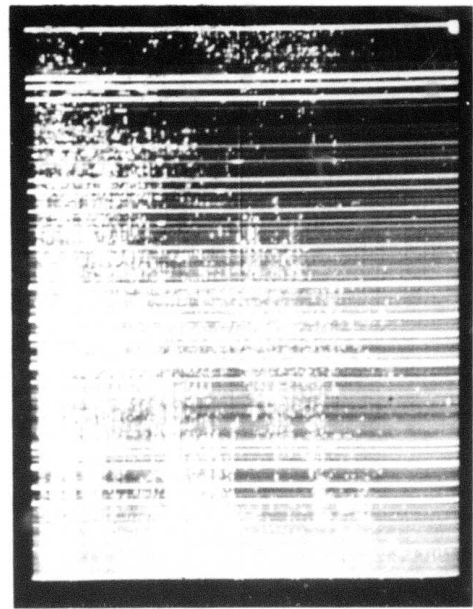
B. Float-Zoned Material

1. Imager Performance

Dark current patterns from imagers on float-zoned material fell into two distinct categories. Devices in the central region of one slice and about the periphery of all slices showed dense patches of dark current lines running in $\langle 110 \rangle$ directions on the slice [Figure 6(a)]. Devices outside of these regions showed a moderately low density of randomly distributed isolated dark current spikes [Figure 6(b)].



(a)



(b)

Figure 6 Dark Current Patterns - Float-Zoned Group

2. X-Ray Topography

The wafer containing the center patch of dark current was selected for study by x-ray topography and transmission electron microscopy. Transmission topographs of this wafer showed that the center patch of dark current was caused by dislocations introduced from the backside of the wafer (Figure 7). Comparison of this topograph with others taken on other slices processed in the same batch showed that the origin of the backside damage was in the process. In contrast to the float-zoned slice, the dislocations induced in the Czochralski slices were confined to the backside and did not propagate to the front surface. It should be noted that the process used has been optimized for Czochralski wafers. Enlargements made from the transmission topographs show the propagation of the dislocations from the backside to the frontside (Figure 8).

The damage introduced in the backside was sufficiently great that the warpage of the slice precluded making a reflection topograph of the entire frontside of the slice. In regions where the backside damage was severe, a large density of dislocations was found in the reflection topographs (Figure 9). In the imager array it was found that these regions correlated well with the regions of dense dark current. There was not a one-to-one correlation between dislocations seen in the topographs and dark current spikes outside this region, however. That is, many dislocations did not act as dark current sources. In regions outside the dislocation patches, no defects were imaged on either transmission or reflection topographs that correlated with the random, moderately low density of dark current spikes reported above.

3. Transmission Electron Microscopy

To date, we have examined only samples taken from the dislocation patch region. Long lengths of dislocation line, very close to the surface, are oriented either parallel or perpendicular to the channels and channel stops. Contrast experiments show that all these dislocations are of the 60°



Figure 7 (220) Transmission Topograph of Float-Zoned Wafer Showing Damage Near Center. Vertical bars result from action of automatic Bragg angle control.

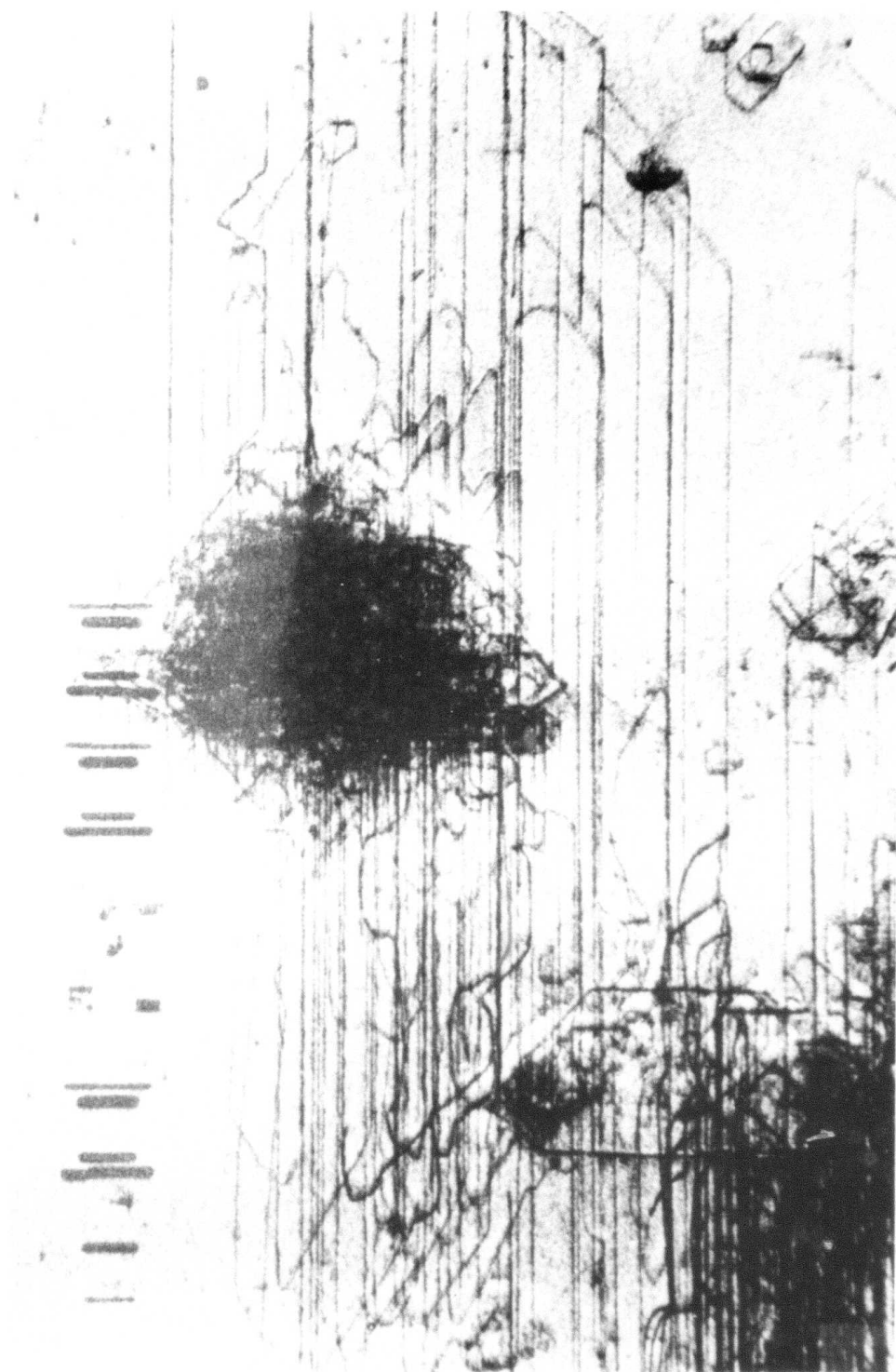


Figure 8 Enlargement of (220) Transmission Topograph Showing Dislocations Emanating from Backside-Damaged Regions

0.5 mm

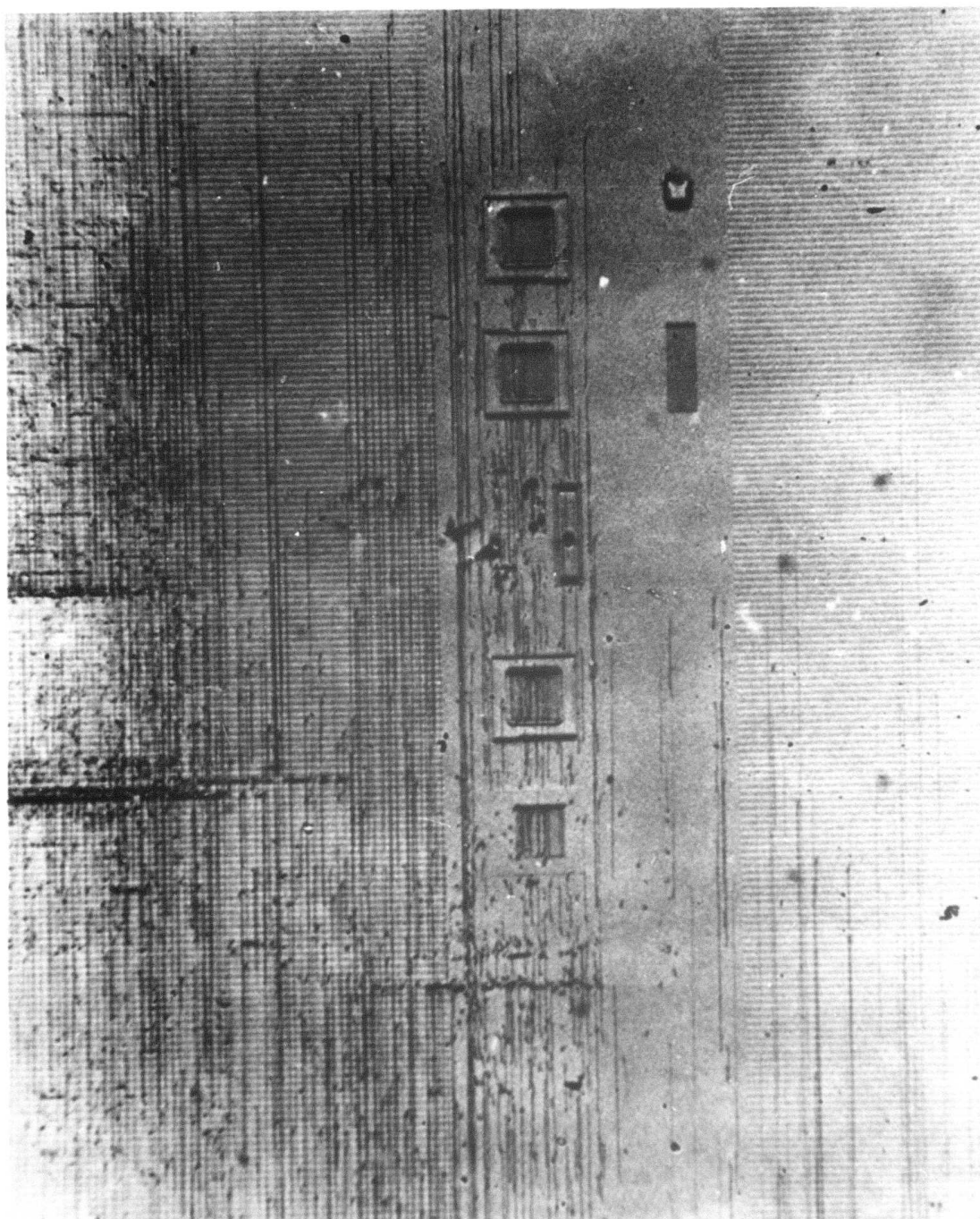


Figure 9 Enlargement of (224) Reflection Topograph of Dislocated Region in Float-Zoned Region

type, i.e., their Burgers vectors are in $\langle 110 \rangle$ directions that do not lie in the plane of the surface (Figure 10).

Occasionally, we find that a dislocation reaction has occurred. Figure 11 illustrates an example where two dislocations, having the same Burgers vector but lying on two different (111) planes (the traces of which are perpendicular in this figure), intersect.

Three of these dislocations have been examined using the weak beam method.² All these dislocations were found to be extensively dissociated; a typical example is shown in Figure 12. The separation at A in this image is 65 Å. Since the partial dislocations lie on an inclined (111) plane, their true separation is approximately 100 Å. At B in this same figure the dislocations also appear to be dissociated by approximately 50 Å. At C there is a constriction where the dislocation is not dissociated.

In addition to the dislocations, a small number of small stacking faults was observed in the channel stop (Figure 13). All the stacking faults were of the same length.

4. Discussion

The long length of dislocation line in the depletion region of the imager clearly originates by a glide process, with the dislocation originating on the back surface. The fact that the dislocation does not exit through the surface, but remains at a shallow depth, is evidently a result of the existence of the thermal oxide. The energy of the system would be lowered if these dislocations moved out through the front surface. For a clean surface, image forces would also tend to pull the dislocation out of the silicon crystal. There must therefore be an inhibiting force caused by the presence of the thermal oxide.

Polysilicon

Aluminum



Channel

Channel Stop

5 μm

Figure 10 Transmission Electron Micrograph of 60° Dislocations Near Front Surface of Float-Zoned Wafer



100 nm

Figure 11 Dark Field Transmission Electron Micrograph of Float-Zoned Wafer Showing Dislocation Reaction. Two perpendicular 60° dislocations moving on two different slip planes, but with the same Burgers vectors, have reacted to form nearly right-angle configuration.

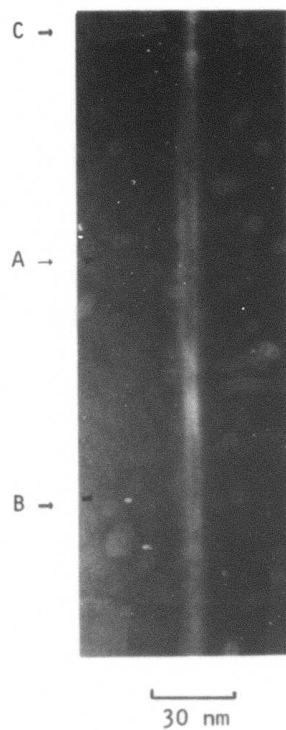


Figure 12 Weak Beam (400) Micrograph of Partially Dissociated Dislocation. Separation in image at A is 6.5 nm, 3.5 nm at B, and no dissociation at C.



Figure 13 Transmission Electron Micrograph of Stacking Fault in Channel Stop of Float-Zoned Wafer

To our knowledge, this is the first report that 60° dislocations are at least partially dissociated in a device. Clearly, this is of fundamental significance in attempting to understand the electrical (or nonelectrical) behavior of dislocations in semiconductors. There have been several reports that dislocations introduced by bending (evidently in float-zoned silicon) are largely dissociated.^{7,9} Our limited observations suggest that this is also the case for slip dislocations in float-zoned material subjected to a complex process, which includes the introduction of oxygen into the dislocation region, and by extension, to any slip dislocation in any material.

The dissociation in Figure 12 proceeds according to the reaction. $\frac{1}{2}\langle 101 \rangle \rightarrow \frac{1}{6}\langle 21\bar{1} \rangle + \frac{1}{6}\langle 112 \rangle$. The two partial dislocations are separated by a stacking fault on the (111) plane. The Burgers vectors and dislocation line orientation of both the perfect and partial dislocations are also found in this same plane. A similar situation exists for any dislocation that is in a configuration to move by a glide process.

The equilibrium spacing of the partial dislocations in "pure" silicon, and with no applied stresses, has been measured. For the 60° dislocation it is between 50 and 60 Å.^{7,9} For this configuration the stacking fault is found to be intrinsic (i.e., the stacking sequence across the fault corresponds to the sequence that would occur if a plane of atoms were removed). At B in Figure 12 this is seen to be the case. The separation at A is anomalously high. There are three possible explanations for this: (1) The stacking fault is extrinsic in this region (i.e., the stacking sequence across the fault corresponds to that if an atomic plane were inserted). Partial dislocations separated by extrinsic faults have been reported to occur when the dislocation is close to the screw (or 0°) orientation.⁹ The extrinsic stacking fault energy is deduced to be lower than the intrinsic stacking fault energy and, hence, the separation of the partials is greater. (2) Oxygen could be adsorbed onto the stacking fault in this region, causing the stacking fault energy to be lowered. (3) Force from the surface of the device could be acting on the dislocation, causing one of the partials to be moved closer to the surface. Obviously, more work is necessary to distinguish which mechanism is at work.

The origin of the stacking faults is also of interest. Note that the size of the stacking faults is about the same as that of the majority found in the Czochralski control group and in the bulk of swirled material. Surface nucleated stacking faults would be much larger. Hence, we surmise that their origin is also from bulk nuclei. If we postulate that the same

unfaulting mechanism is at work in this material, then the density of dark current defects in the imager should be related to the stacking fault density in the channel stop. In this material, the channel stop stacking fault density is about 10 to 20% of that found in the control Czochralski, and hence the dark current defect density should be about 10 to 20% of that of the control Czochralski group. This is indeed the case, suggesting that the random distribution of dark current defects in the float-zoned material arises from unfaulted stacking faults. We will examine additional devices to verify this observation.

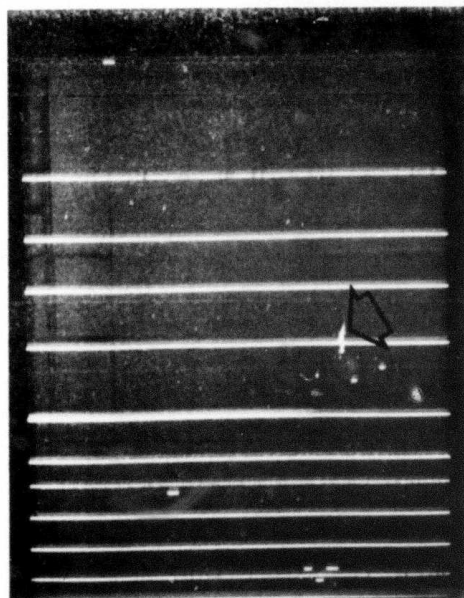
C. Czochralski - Group I

1. Imager Performance

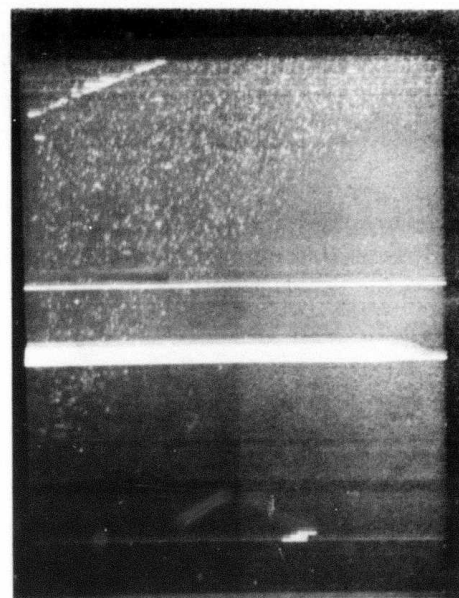
Dark current defect patterns in imagers on this material fell into two classifications. Near the periphery of the wafer there was a high density of defects in a discernible pattern [Figure 14(a)]. Devices in the center of the wafer showed a very low density of dark current defects. These frequently extended over more than one pixel [Figure 14(b)]. These slices had backside mechanical damage by sandblasting with glass beads over half the slice. There was a slight reduction in the defect density for imagers over the backside damaged portion of the slice. (See Table 1 of the last quarterly technical report.¹)

2. X-Ray Topography

There was no correlation between the reflection topographs and the high density of dark current defects found near the periphery of the wafer. Near the end of the wafer, however, there was a nearly one-to-one correlation between dark current spikes and dislocation cluster defects observed in reflection topographs. Two typical examples of these are shown in Figure 15. In Figure 15(a) it will be seen that most of the dislocations are electrically inactive. Only the dislocation indicated by the arrows is a source of dark current. Similarly, the dislocations emanating from the round defect in

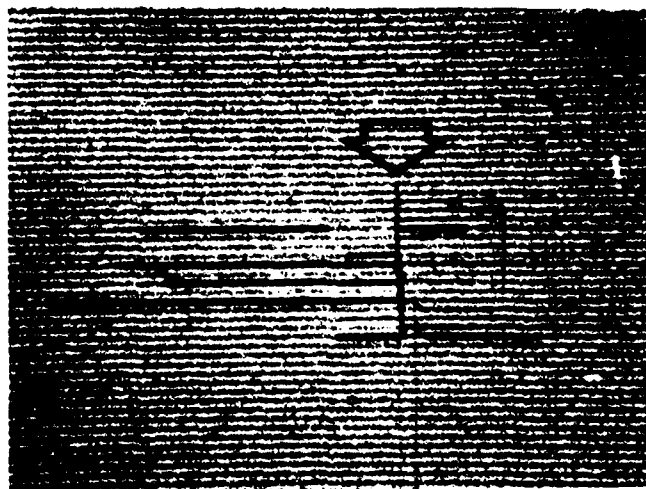


(a)

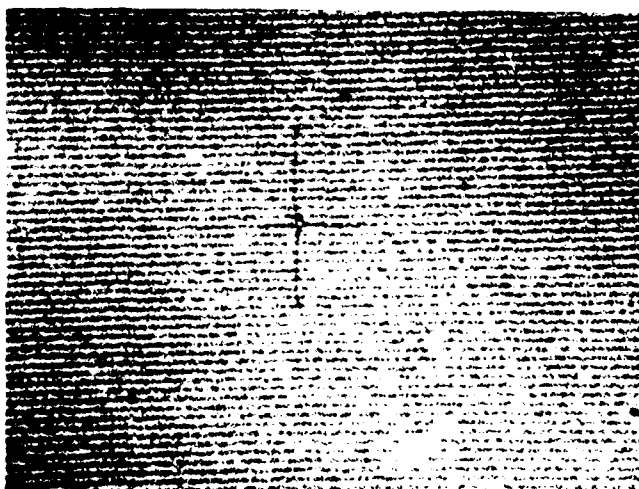


(b)

Figure 14 Dark Current Patterns - Czochralski Group 1. Defect at arrow in (b) is shown in topograph, Figure 15 (a).



(a)



(b)

0.5 mm

Figure 15 (224) Reflection Topographs of Defects in Czochralski Group 1. Only the dislocation indicated by arrow in (a) is a dark current source, while in (b), only the spot in the center of the defect is a dark current source.

Figure 15(b) were not dark current sources. The round defect was a very intense source of dark current and led to blooming down the channel and into several adjacent channels.

Transmission topographs also showed that there was a region of bulk "swirl" precipitation near the center of the wafer. Devices lying over this swirl precipitation were those in which the density of defects was lowest.

D. Czochralski - Group 2

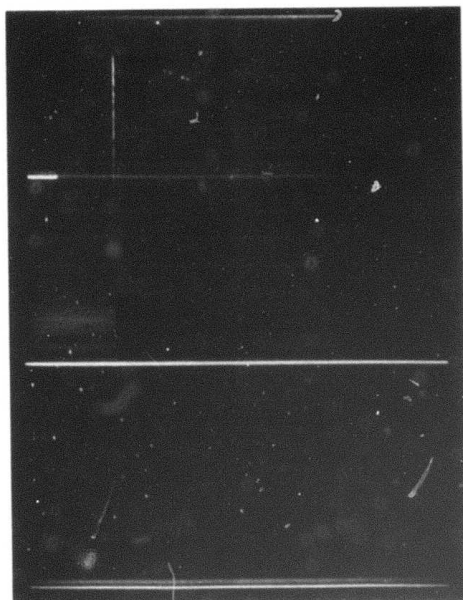
1. Imager Performance

The dark current spike behavior of this material was similar to that of Czochralski - Group 1. Imagers at the periphery of the slice had a moderately high density of weak dark current spikes, many of which were in a discernible pattern (Figure 16), while those near the center of the slice had a relatively low density of dark current spikes. Backside mechanical damage by glass bead sandblasting had no discernible effect on the dark current spikes.

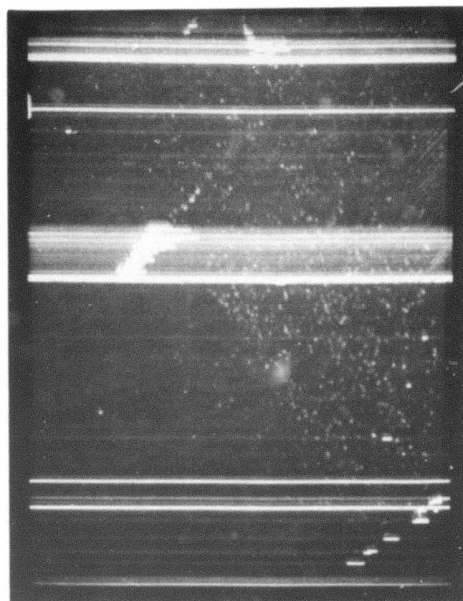
2. X-Ray Topography

Only a few defects were imaged in reflection topography. These defects correlated with the more intense dark current spikes near the center of the slice. A typical example is shown in Figure 17, which correlates with the indicated dark current defect in device 3 of Figure 16. From the pattern of dark current defects of this type that were visible in the imagers and the topographs, it appears that their origin is frontside damage caused by handling of the slice before processing. (The backside damage was applied after the completion of the frontside polish.) No defects were imaged in reflection topography that correlated with the moderate number of dark current defects visible in some of the imagers.

Device 1



Device 2



Device 3

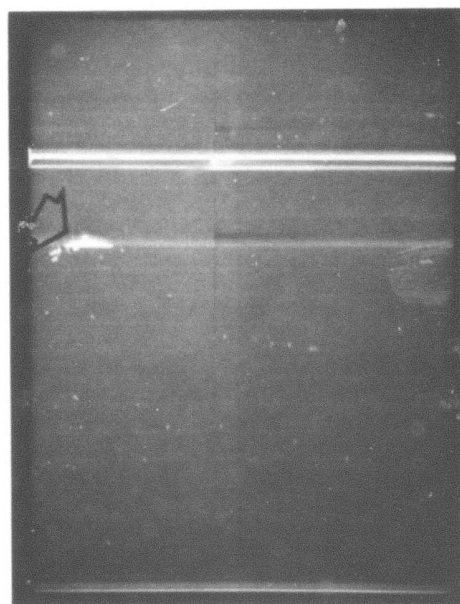
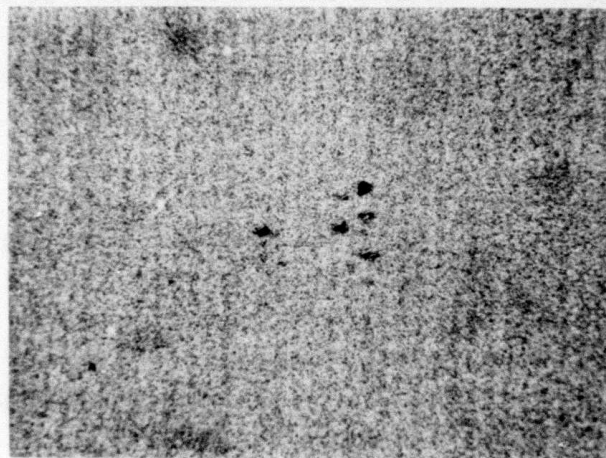


Figure 16 Dark Current Patterns of Three Adjacent Devices, Czochralski Group 2
Defect at arrow in device 3 is shown in topograph, Figure 17.



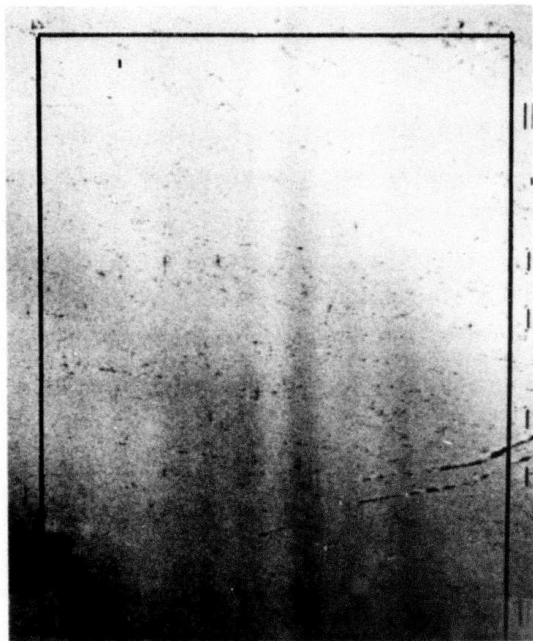
100 μm

Figure 17 224 Reflection Topograph of Dark Current Defects in Czochralski Group 2. Defect is marked in Figure 16, device 3.

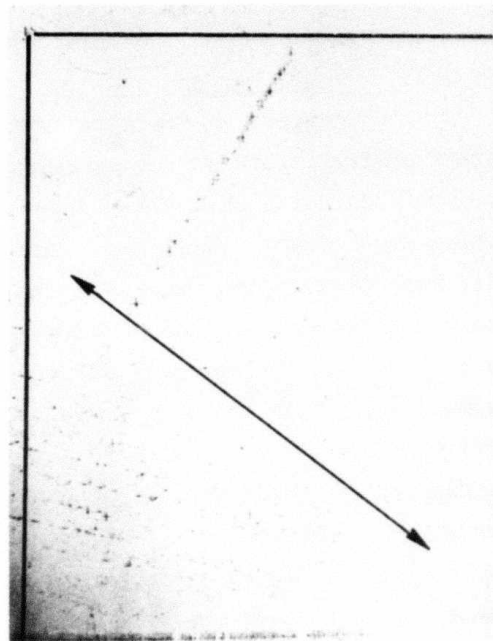
Transmission x-ray topographs showed that there was a region of bulk "swirl" precipitation in this material. There was a general, but not specific, correlation between the occurrence of this precipitation and imagers with low dark current defect density. Figure 18 is an enlargement of a transmission topograph of devices 1 and 2 of Figure 16. It will be noticed that the edge of the band of dark current defects visible in device 2 parallels the swirl band visible in the topograph. The band of dark current defects is offset from the edge of the swirl by approximately 1 mm, however.

3. Discussion

It is important to establish the exact relationship between the dark current spikes and the bulk "swirl" precipitates in this wafer. Two possibilities exist: (1) that the swirl precipitate serves as a "getter" for these defects, or (2) that the growth conditions in the boule favor defect formation outside the region of the swirl, while slightly different growth conditions lead to a suppression of defect nuclei in the region of the swirl. If the former were the case in this wafer, then comparison of the transmission topograph and device 2 of Figure 16 shows that the "gettering" range of the swirl is of the order of 1 mm. Now in device 1 of this same figure there are also several defects with the same dark current characteristics. Reference to the transmission topograph, Figure 18, shows that these defects lie over a region of swirl precipitate that is somewhat less intense than the most intense regions, but still considerably more intense than the swirl precipitation within 1 mm of the band of defects in device 2. In addition, these defects lie within 1 mm of the most intense swirl regions. If these defects in device 1 are in fact the same as the defects in device 2, as seems most probable, and if a gettering mechanism were at work, then the defects in device 1 should be absent. The distribution of the dark current defects in this slice thus appears to be a result of varying growth conditions in the boule when the crystal is grown.



Device 1



Device 2

Figure 18 (220) Transmission Topograph of Two Devices Whose Dark Current Signature is Shown in Figure 16. Bulk swirl precipitation region is the darkening most noticeable in device 1. Arrow in device 2 indicates line above which there are numerous dark current defects. Black spots and lines on topograph are defects on the backside of the devices.

E. Czochralski - Group 3

This group had a $\langle 100 \rangle$ flat.

1. Imager Performance

Imagers on this material behaved similarly to imagers on Groups 1 and 2 in that those at the periphery of the wafer had a high density of dark current defects, while those near the center had a much lower defect density. There were several significant differences, however. The density of defects in some imagers was extremely high: of the order of 10% of the pixels had dark current spikes. In addition, the density of defects near the center of the slice was higher than for devices from the center of Groups 1 and 2. In some cases, there was a definite "swirl" pattern to the dark current spikes (Figure 19). Backside mechanical damage by glass bead sandblasting appeared effective in removing a large number of dark current spikes. For example, while the worst-case imagers on the undamaged side of the slice had approximately 10% of their pixels with a dark current spike, on the damage side the worst case was 1%.

2. X-Ray Topography

No defects were imaged in reflection topography on this material. Transmission topographs showed that this material also contained a central region of bulk "swirl" precipitate.

3. Transmission Electron Microscopy

Samples for transmission electron microscopy were taken from the central high defect regions of the imagers illustrated in Figure 19. No defects were imaged. These same samples were successively etched-back from the front surface in 2 μm increments and again examined in the electron microscope. This procedure showed there were no defects in the outer 5 μm of the devices.

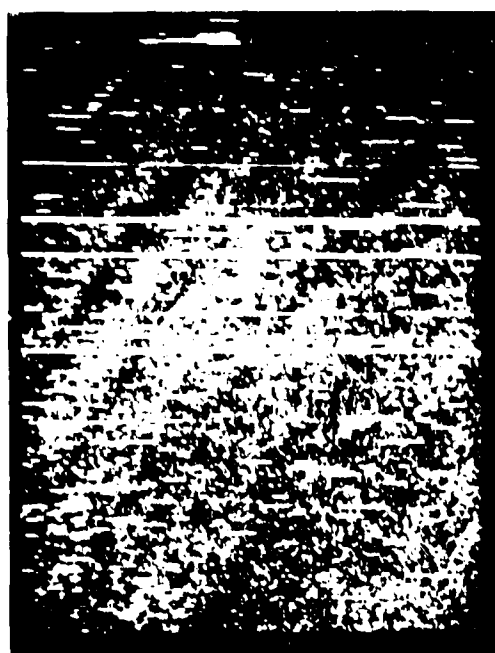


Figure 19 Dark Current Pattern in Czochralski Group 3

Samples taken from high defect regions of other devices had the dislocation clusters shown in Figure 20. Limited contrast experiments in the electron microscope showed that the long dislocation line in these clusters, which was oriented in a $\langle 110 \rangle$ direction, was of pure edge type. All these dislocation clusters were located in the channel stop.

An additional type of defect was seen in the channels (Figure 21). These defects were located underneath the aluminum electrode and primarily near the edge of a neighboring polysilicon electrode. Their nature is not clear at this time.

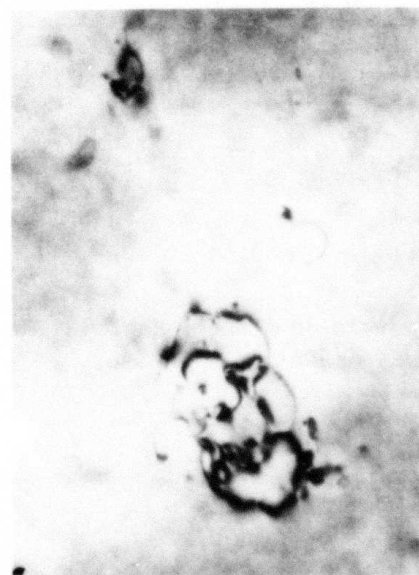
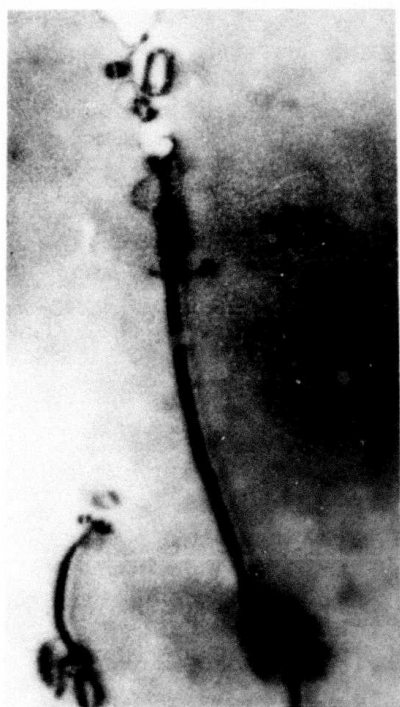
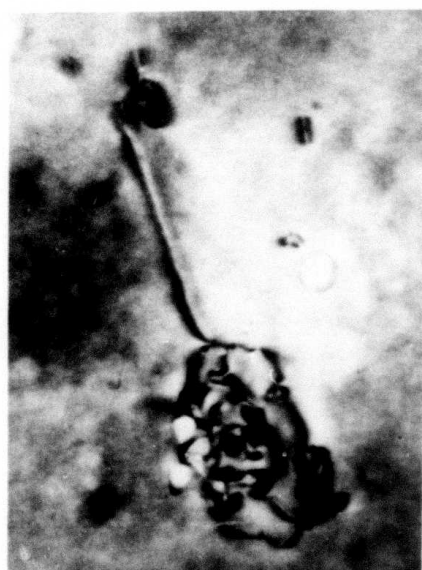
4. Discussion

The fact that the defects that cause dark current spikes in the imager were not imaged in the electron microscope indicates that they are surface or interface defects. In our experimental procedure, the overlying polysilicon, aluminum, and oxide are removed by etching in a dilute HF solution. There is evidence to suggest that this etch also lightly attacks the silicon, possibly removing as much as a few hundred Å from the surface. This is evidently a result of dissolved oxygen in the etch solution. We have developed an improved etch to eliminate this oxygen, and the experiments are in the process of being repeated. If the defect is truly an interfacial defect, then it may be necessary to leave some oxide on the device so the interface may be examined in the electron microscope.

The defects that were imaged (Figure 20) appear to have originated from a stacking fault.

F. Results of ISS Backside Damage Tests

Ten slices of material from Czochralski - Group 1 were treated with Impact Sonic Stressing (ISS) and returned to us for processing and evaluation. Five of these slices were matched with five untreated slices taken from



0.5 μm

Figure 20 Dislocation Clusters in Channel Stop Region. The longer dislocation lines are pure edge.



100 nm

Figure 21 Defects in Channel Region. The defect lines are oriented in $\langle 100 \rangle$ directions.

neighboring positions in the boule, and sent through the standard imager process.

X-ray transmission topographs were taken of the finished slices (Figure 22). This superposition of device geometry with the damage pattern reveals that there are six devices at the slice center where the damage pattern is uniform across the whole device. At first sight, it would seem that one way to judge the effectiveness of ISS would be to compare the quality of these six devices with that of devices on the same slice that come from the outer, undamaged part. Such a comparison is invalid, however, because the slices that were not ISS-treated do not display a uniform density of dark current spikes (see Section II.C). Rather, the efficacy of ISS must be judged by a comparison of the center six devices on ISS-treated material with those on untreated material.

Typical results for the untreated control slices are shown in Figure 23. Here, two adjacent devices from two slices illustrate the range of dark current spikes found on the center six devices. Typical devices from the ISS-treated slices are shown in Figure 24. From these results, we conclude that the ISS treatment does not lead to significant improvement in the density of dark current spikes on this material.

It should be noted, however, that the processing of these slices included gettering steps as a standard feature. The second set of five slices now in process will bypass these steps. This will allow a determination of whether or not these gettering steps mask the effect of the ISS treatment. In addition, ISS-treated slices of material from Czochralski - Group 3 (where the effect of glass bead backside damage showed positive results), and from the float-zoned group will be processed without these process gettering steps.

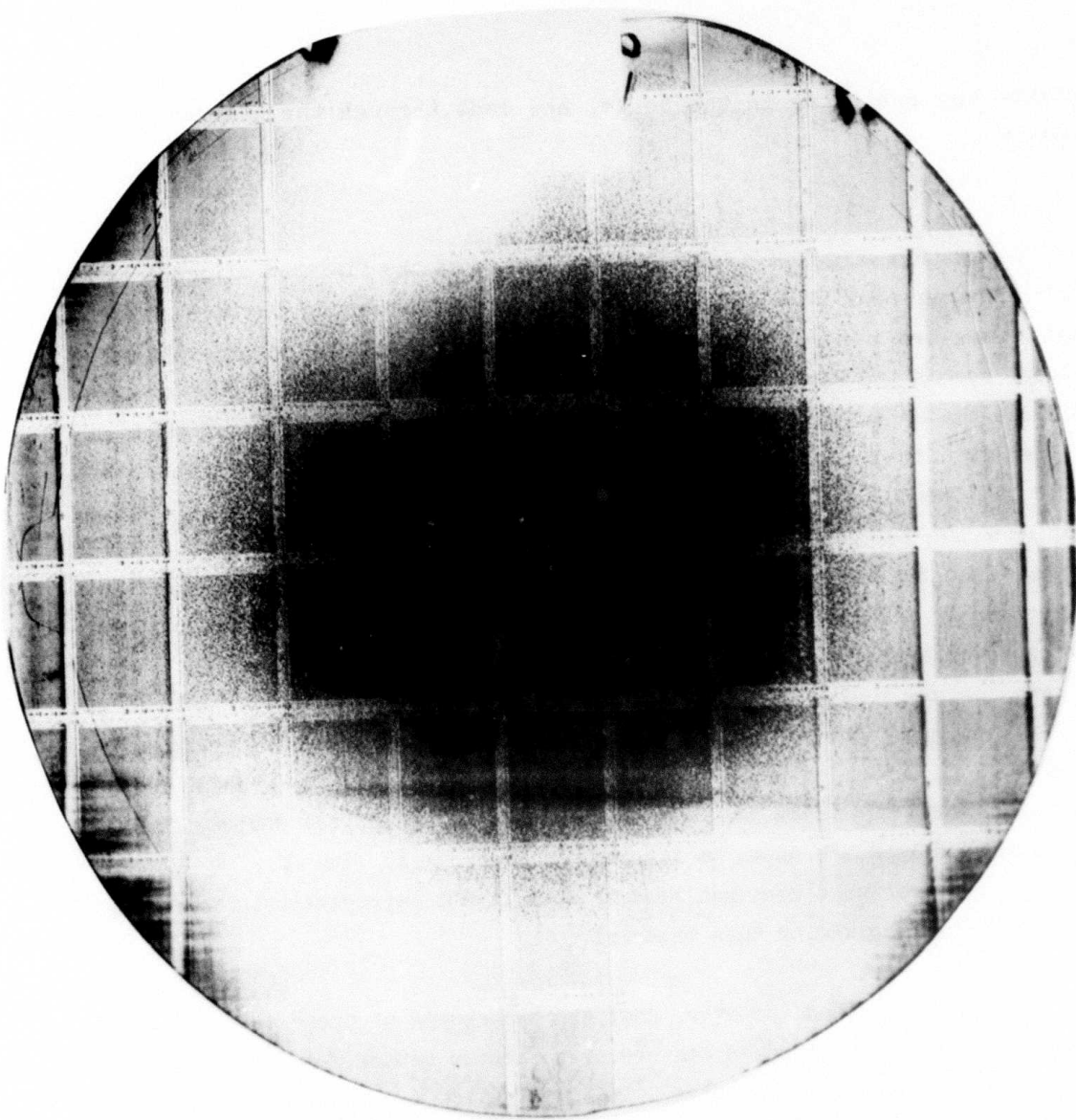


Figure 22 (220) Transmission Topograph Showing Pattern of ISS Backside Damage

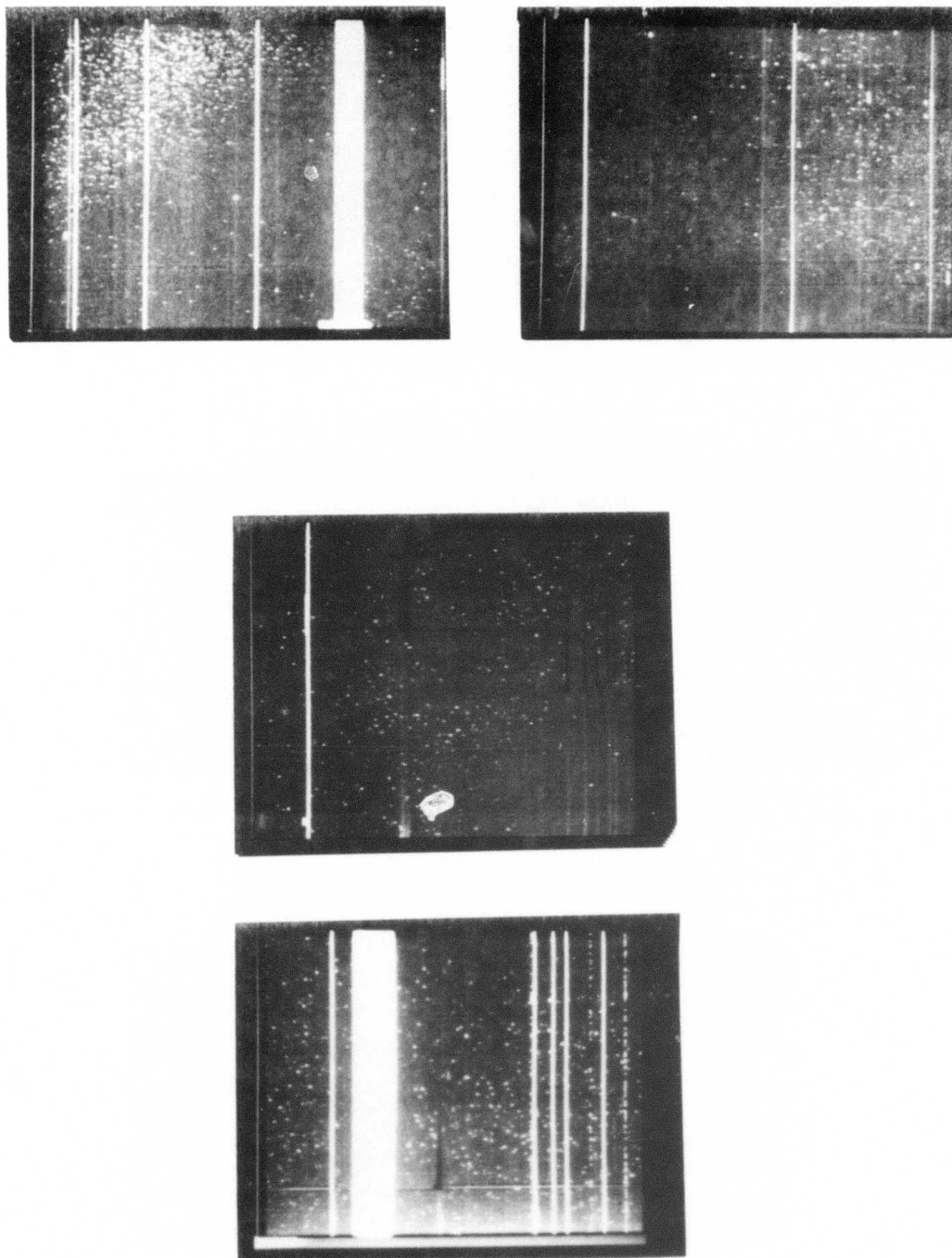


Figure 23 Dark Current Readout of Typical Devices on Control Slices Not Treated with ISS

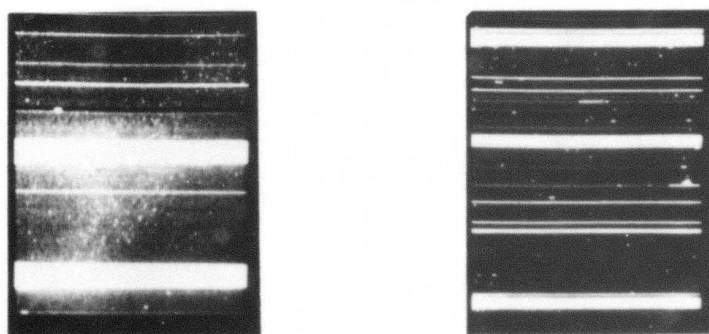
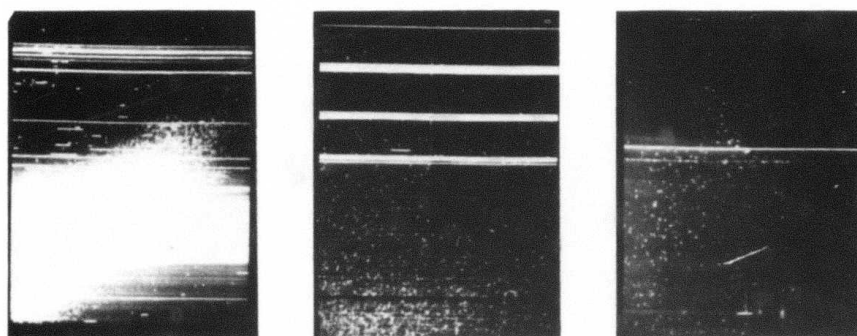
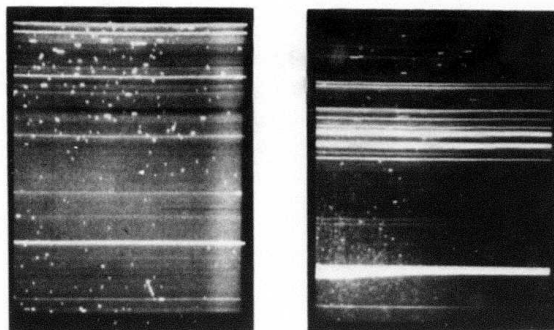


Figure 24 Dark Current Readout of Typical Devices from Slices Treated with the ISS Backside Damage

G. Relationship of Total Dark Current and Dark Current Spike Density

The CCD imager that we are using is essentially an array of 80,000 silicon MOS capacitors on a piece of silicon with a convenient method of organizing and displaying the resulting data. Each of these capacitors has an area approximately 1 mil^2 . If the outputs of these capacitors are summed over the entire array, then the resulting dark current should be analogous to a large-area MOS capacitor such as is frequently used in material evaluation.

The dark current contribution to each pixel of the imager will consist of two components: the bulk dark current and a spike dark current arising from a crystallographic defect, if present. The resulting total dark current obtained by summing over all of these will consist of two similar components, a bulk dark current, which is an average over the array, and a spike dark current, which is also an average over all the array. If, for example, 1% of the pixels have a dark current spike that has a dark current five times that of the bulk dark current, then the total dark current will consist of the bulk dark current plus an additional 5% due to the dark current spikes. Obviously, an imager containing the dark current spikes would exhibit a dark current 5% greater than one that was spike-free if the bulk dark current in the two were the same.

Our data suggest that, from device to device, the bulk dark current may vary more than the average spike dark current. For example, in material from Czochralski - Group 2, the dark current in imagers over the undamaged backside was an average of 12.0 nA/cm^2 , while those over the backside damage had an average dark current of 7.8 nA/cm^2 . At the same time, the dark current spike density of imagers on both the damaged and undamaged regions was comparable. In Group 1, a much more noticeable reduction in dark current spike density resulted in a smaller decrease in total dark current.

It thus appears that backside gettering has two effects: (1) in some cases to reduce the number of crystalline defects that produce dark current spikes, and (2) to reduce the bulk dark current. This latter reduction is probably associated with the removal of atomistic defects, such as impurities, silicon self-defects, etc., which are evidently fairly uniformly distributed throughout the device.

Because of the noncorrelation between total dark current and dark current spike density, particularly when the dark current is of the order of 10 nA/cm^2 or less, it is impossible to relate macroscopic MOS capacitor data to dark current spike behavior. It is therefore necessary to study these defects using a CCD imager, or an MOS capacitor of comparable size.

H. Role of Transition Metal Impurities

There has been considerable speculation in the literature that electrical activity of crystallographic defects arises from transition metal impurities associated with the defects (see for example, References 10 through 12). Evidence in support of this speculation has been rather sparse. There are three conceivable ways in which transition metal impurities could cause electrical activity: by precipitation on crystallographic defects (decoration); by adsorption onto crystallographic defects without precipitation; and as a nucleation agent for the formation of crystallographic defects, which grow by a mechanism independent of the transition metal impurity. Of these three mechanisms, our experiments are capable of detecting only the first.

So far, we have seen no precipitates in any of the CCD imager arrays. Since in the weak beam experiments the dislocation image size is under 30 \AA , we can positively say that if a precipitate is present on the dislocation, it must be smaller than 30 \AA in diameter. In the few cases where we have seen precipitates (on samples where extensive unfaulting of stacking faults

occurred, and on dislocation loops in bulk swirl regions), the precipitates have been of the order of 100 Å diameter. Again it should be emphasized that these samples have not been taken from the active region of a processed device.

SECTION III

DISCUSSION

The most interesting observations from the standpoint of producing CCD imagers with low dark current spike density is that the density of dark current spikes is frequently lower in regions where the wafer has bulk swirl precipitation than in regions where it does not (Czochralski - Groups 1, 2, and 3, as well as our previous report on swirled imagers). Evidently, the occurrence of bulk stacking faults is not affected by the presence of bulk swirl (Czochralski Control), nor is the occurrence of dislocation clusters (Czochralski - Group 1).

The question of whether this defect-free region is a result of an intrinsic gettering process or merely reflects crystal growth conditions that result in a defect-free process is important, but our data are insufficient to determine the answer. Assuming that the bulk swirl region is one that, due to the microscopic growth conditions, is high in oxygen, then, as a result of the segregation coefficients of oxygen and carbon, it will also be a region that is low in carbon. Similarly, it will be a region in which the microscopic growth rate is different from that of neighboring regions. The question to be determined is which of these three factors, low carbon, high oxygen, or favorable growth rate, or which combination of these factors, leads to the elimination of dark current defects in the imager.

There is some information in the literature on the origin of bulk stacking faults. Evidently, a nucleation heat treatment is required for their formation.¹³ 700°C has been reported to be an effective temperature for this process.¹³ It is interesting to note that most commercial Czochralski materials undergo a stabilization bake in this temperature region to remove the oxygen donors that are formed in the vicinity of 450°C, and thereby stabilize the wafer resistivity. Similarly, there are some indications that

carbon is associated with the formation of bulk stacking faults, acting as a heterogeneous nucleation agent.^{14,16} These stacking faults could presumably be eliminated by either eliminating the temperatures in the nucleation range, or reducing the amount of carbon below that required for nucleation. The former approach is questionable, since a wafer will always see temperatures in the nucleation range for a brief period during cooldown. This may be a sufficient time for the nucleation to take place. Thus, it appears that reduced carbon is required to suppress the formation of stacking faults, although more work is needed to tie down the role of carbon in stacking fault formation.

Our observations on dislocations whose origin is a slip process show that only a small number of these act as dark current sources. Although we have insufficient data to make a quantitative statement, the previously reported figure of 5%^{17,18} of these dislocations that are electrically active is in qualitative agreement with our data. It is important to establish the reason for the electrical activity of these dislocations. It is significant that we do not see precipitates on the dislocation in the active regions of a device. While adsorbed impurities on a dislocation core may affect the magnitude of electrical activity, it is unlikely that this is the explanation of why some dislocations in a region are electrically active while most are not. This follows from the fact that the reason impurities would be adsorbed is that the chemical potential of an impurity on the dislocation core is lower than the chemical potential of the impurity in solution. Because of the fast diffusion coefficients of most impurities, the impurity concentration on all dislocations in a given region should be the same.

An interesting possibility for the observed anomalous behavior of dislocations lies in our observation that slip dislocations are in fact partially dissociated in the active region of a CCD imager. We observe that the dislocation resulting from the unfauling of a stacking fault that is

electrically active is not dissociated into two partial dislocations. Reports in the literature indicate that slip dislocations are largely dissociated.^{8,9} In limited experiments we have observed this in the active region of the device. Thus, it is possible to speculate that it is the undissociated dislocation that is electrically active. From our data, a dislocation would cause a dark current spike if from 0.5 to 1 μm of undissociated dislocation were located in a depletion region of approximately $1500 \mu\text{m}^3$. Based on measurements on the devices we have been using, it is possible to estimate that the leakage current of an undissociated dislocation is of the order of 1 nA/cm of dislocation line.

SECTION IV

PLANS

In the final quarter of this program, characterization of the defects by Transmission Electron Microscopy will be completed. This will include chemical characterization using the x-ray analytical capabilities of our new Scanning Transmission Electron Microscope. It is also planned to attempt one-to-one correlations between dark current spikes and defects visible in the electron microscope.

REFERENCES

1. H. F. Schaaake, A. J. Lewis, and C. G. Roberts, Texas Instruments Incorporated, "Characterization of Electrically Active Defects in Si Using CCD Image Sensors," Quarterly Technical Report No. 4 for Contract No. N00173-76-C-0280, September 1977.
2. D. J. H. Cockayne, I. L. F. Ray, and M. J. Whelan, *Phil. Mag.* 20, 1265 (1969).
3. H. F. Schaaake, A. J. Lewis, and C. G. Roberts, Texas Instruments Incorporated, "Characterization of Electrically Active Defects in Si Using CCD Image Sensors," Quarterly Technical Report No. 3 for Contract No. N00173-76-C-0280, June 1977.
4. G. A. Rozgonyi, S. Mahajan, M. H. Read, and D. Brasen, *Appl. Phys. Lett.* 29, 531 (1976).
5. I. R. Sanders and P. S. Dobson, *Phil. Mag.* 20, 881 (1969).
6. H. Hashimoto, H. Shibayama, H. Masaki, and H. Ishikawa, *J. Electrochem. Soc.* 123, 1899 (1976).
7. I. L. F. Ray and D. J. H. Cockayne, *Phil. Mag.* 22, 853 (1970).
8. I. L. F. Ray and D. J. H. Cockayne, *Proc. Roy. Soc. A* 325, 534 (1970).
9. A. Gomez, D. J. H. Cockayne, P. B. Hirsch, and V. Vitek, *Phil. Mag.* 30, 105 (1975).
10. C. J. Varker and K. V. Ravi, *Semiconductor Silicon 1977*, H. R. Huff and E. Sirtl, eds. (Electrochemical Society, New York, 1977), p. 785.
11. R. Ogden and J. M. Wilkinson, *J. Appl. Phys.* 48, 412 (1977).
12. G. Rozgonyi and R. A. Kushner, *J. Electrochem. Soc.* 123, 570 (1976).
13. P. E. Freeland, K. A. Jackson, C. W. Lowe, and J. R. Patel, *Appl. Phys. Lett.* 30, 31 (1977).
14. T. Abe, private communication.
15. A. J. R. de Kock, *Semiconductor Silicon 1977*, loc. cit., p. 508.
16. H. Föll, V. Gösele, and B. O. Kolbesen, *Semiconductor Silicon 1977*, loc. cit., p. 565.
17. C. L. Claeys, E. E. Laes, G. J. Declerck, and R. J. Van Overstraeten, *Semiconductor Silicon 1977*, loc. cit. p. 773.

18. S. Kawado, Y. Hayafuji, and T. Adacki, 1975 Fall Meeting of the Electrochemical Society, Extended Abstracts Volume 75-2 (Electrochemical Society, New York, 1975), p. 477.